

Effect of Continuous Cooling Transformation Variations on Numerical Calculation of Welding-Induced Residual Stresses

Three continuous cooling transformation (CCT) diagrams for S355J2 steel were employed to study the effect of CCT variations on calculated residual stresses

BY J. CARON, C. HEINZE, C. SCHWENK, M. RETHMEIER, S. S. BABU, AND J. LIPPOLD

ABSTRACT

Continuous cooling transformation (CCT) behavior affects the transient state of material properties employed in a numerical welding simulation, having a direct influence on the developing stress state. Three different CCT diagrams for S355J2 steel were employed to understand the influence of variations in CCT behavior on the numerical calculation of welding-induced residual stresses. The CCT diagrams were constructed from transformation data contained in the Sysweld software database, measured dilatometric data from Gleeble experiments, and transformation data calculated from the JMatPro software. The calculated transverse and longitudinal residual stress distributions provided a qualitative correlation only in comparison to experimental measurements, with the largest deviation occurring near the weld interface. Overall, the results indicate a weak dependency of the calculated residual stresses due to anticipated CCT variations. The most significant effect on the calculated residual stresses was shown to be related to the proportion of formed martensite. It is suggested that CCT data of approximate accuracy is sufficient for reliable calculation of welding-induced residual stresses.

Introduction

During welding, residual stresses are developed due to the local plastic deformations created by the steep thermal gradient that occurs in the weld zone from localized heating and cooling (Ref. 1). Phase transformation strains, which are created from differences in crystal structure and mechanical properties, also contribute to the evolution of residual stresses during welding (Ref. 2). Both the diffusive and displacive phase transformation mechanisms are often accompanied by substantial strains, which greatly exceed elastic strain values (Ref. 1). Residual tensile stresses result in unwanted deformations of the welded component, increase the susceptibility to hydrogen-induced cold cracking, and also combine with tensile stresses experienced during service to pro-

mote brittle fracture, fatigue failure, and stress corrosion cracking (Ref. 3).

An historical account of research relating to weld residual stresses and distortions is provided by Dong (Ref. 4). One of the initial studies to use the finite element (FE) method to study welding-induced residual stresses dates back to Ueda et al. in 1977 (Ref. 5). In recent years, the on-cooling phase transformation behavior has been integrated in FE simulations of steel (Refs. 6–10). These studies have all shown the strong effect of the austenite to martensite transformation on the final residual stress state. The influence induced by the volume expan-

sion has been found to be more significant than that due to the yield strength change (Refs. 7, 10). Ferro et al. (Ref. 8) isolated the effects of volume change and transformation plasticity in a numerical simulation of laser beam welding of steel plate. The overall effect of phase transformations was to generate compressive longitudinal stresses in the fusion zone and to shift the location of the maximum tensile stress in the heat-affected zone (HAZ). In an investigation of the influence of thermophysical and thermomechanical material properties on the numerical calculations, thermal expansion was shown to have the most significant influence; giving a direct proportional variation of the calculated distortions in both the longitudinal and transverse directions (Ref. 11). In addition to the simulation results, experimental development of new filler metal compositions has demonstrated that a lower martensitic transformation temperature reduces residual stresses by allowing the expansion associated with the martensite transformation to compensate for the accumulated thermal contraction strains (Ref. 12). A review of the metallurgical issues and modeling challenges associated with calculation of welding-induced residual stresses, with respect to ferritic power plant steels, is given by Francis et al. (Ref. 13).

While the effect of on-cooling phase transformations and material properties variations have been established, information regarding the effect of variations in CCT behavior has not yet been considered. Given the relatively wide composition ranges specified for certain alloys and the heat-to-heat composition variations that do occur, significant differences in CCT behavior can be expected. In steels it is well known that the martensite start (M_s) temperature is a strong function of the carbon content, and that the ferrite and bainite transformation kinetics are known to be

KEYWORDS

Continuous Cooling Transformation Diagrams
Residual Stresses
Gas Metal Arc Welding
C-Mn Steels
Welding Simulation

J. CARON, S. S. BABU, and J. LIPPOLD are with Welding Engineering Program, The Ohio State University, Columbus, Ohio. C. HEINZE, C. SCHWENK, and M. RETHMEIER are with Division V5 Safety of Joined Components, Federal Institute for Materials Research and Testing (BAM), Berlin, Germany.

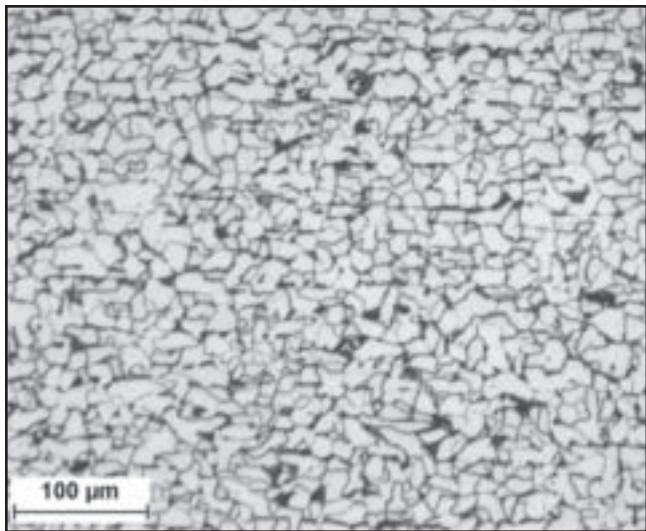


Fig. 1 — Microstructure of S355J2 plate material following heat treatment and prior to welding. Etched with 2% Nital.

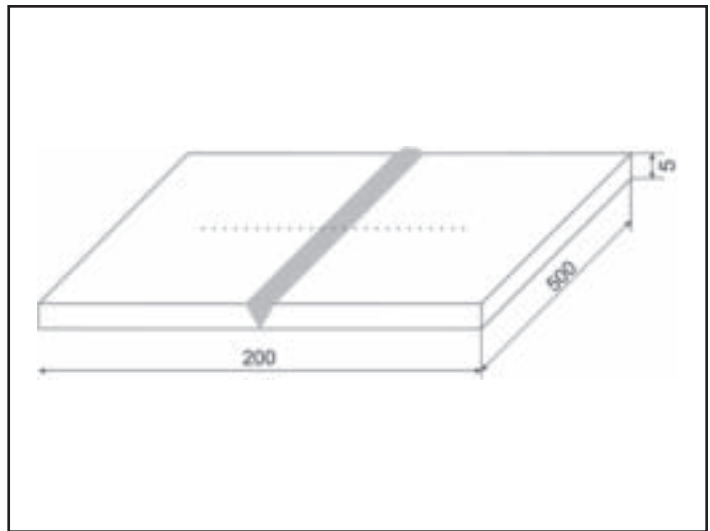


Fig. 2 — Experimental weld schematic with plate dimensions in mm. Dotted line indicates location of residual stress measurements.

sensitive to alloying elements that decrease the driving force for austenite decomposition, particularly carbon, manganese, nickel, and chromium (Ref. 14). Also contributing to variability are the different experimental and computational methods that are used to determine CCT diagrams. In welding, austenite inhomogeneity often occurs due to the inability of alloying elements and precipitates to completely solutionize during the rapid weld thermal cycle. Thus, CCT diagrams constructed from short-time holds at high temperatures in the austenite region are more appropriate for determining HAZ CCT behavior than the conventional CCT procedure of holding on the order of an hour at a temperature slightly above the fully austenite (A_{C3}) temperature (Ref. 15).

Knowledge of the effect of CCT variations on the numerical calculation of residual stress would enable an estimation of the deviations in the calculated results that can be expected when using phase transformation data of unknown or reduced accuracy.

Furthermore, a detailed knowledge about the important aspects of the CCT behavior helps to define the quality and the suitability of a CCT diagram with respect to the calculation of welding-induced residual stresses. This information would allow an estimation of the required accuracy of CCT data and is also necessary to benchmark the quality of the numerically calculated residual stresses when considering phase transformation effects.

Experimental Procedure

The steel used for the welding experiments was S355J2 (1.0577), a German standardized plain-carbon fine-grained construction steel with a minimum yield strength of 355 MPa (51 ksi). The chemical composition and specified minimum mechanical properties for S355J2 plate material thicknesses ≤ 16 mm (0.63 in.), as specified in the German DIN EN 10025 standard (Ref. 16), are provided in Tables

1 and 2, respectively.

The chemical composition of the plate material used in the welding experiments was determined through spark emission spectroscopy. The average composition from three analyses is provided in Table 3. A tensile test conducted on the base plate confirmed the yield strength and ultimate tensile strength to be 363 MPa (53 ksi) and 488 MPa (71 ksi), respectively. The average hardness of the as-received material was determined to be 144 HV10.

A stress-relief heat treatment, consisting of heating to 570°C (1058°F) at 5°C/min, holding at temperature for 3.5 hours, and furnace cooling to ambient temperature, was applied to the plate material before welding to reduce any pre-existing residual stresses. Figure 1 shows the microstructure of the experimental plate material following the stress-relief heat treatment, which consisted of ferrite and pearlite with an average hardness of 138 HV10, with no noticeable differences in microstructure compared to the as-

Table 1 — Nominal Chemical Composition of S355J2 Plate Material according to DIN EN 10025-2:2004 (values in wt-%)

C	Si	Mn	P	S
≤ 0.20	≤ 0.55	≤ 1.60	≤ 0.035	≤ 0.035

Table 2 — Specified Minimum Mechanical Properties of S355J2 Plate Material according to DIN EN 10025-2:2004

Yield Strength (MPa)	Tensile Strength (MPa)	% Elongation	V-Notch Impact Energy (J)
355	470–630	17	27 (at -20°C)

Table 3 — Measured Chemical Composition of S355J2 Plate Material (values in wt-%)

C	Si	Mn	P	S	Cr	Mo	Ni	Al
0.14	0.20	0.67	0.00823	0.012	0.033	< 0.01	0.0354	0.0354
Nb	Ti	V	W	Co	B	N	Cu	Fe
0.005	0.0023	0.00393	< 0.01	< 0.01	0.0003	0.007	0.0221	balance

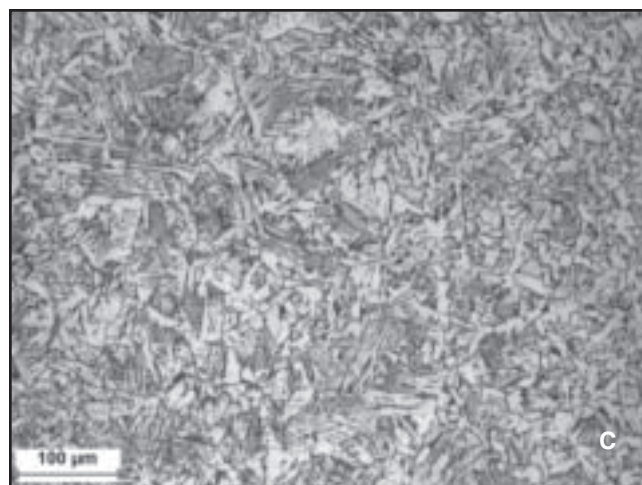
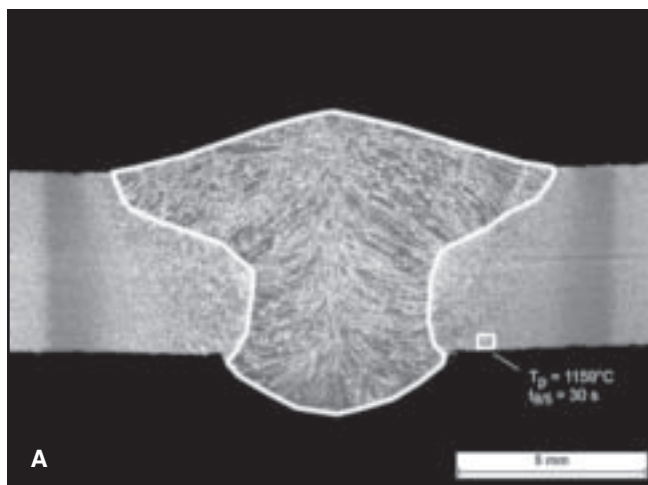


Fig. 3 — A — Macrosection of experimental weld joint with weld interface highlighted; B — microstructure at weld interface, weld metal to the left, coarse-grained heat-affected zone (CGHAZ) to the right; C — HAZ microstructure from location noted in (A). Etched with 2% Nital.

received material.

The individual plate dimensions for the welding experiments were 500 mm (19.7 in.) length, 100 mm (3.93 in.) width, and 5-mm (0.197 in.) thickness containing a 60-deg V-groove with joint edges milled. A single-pass complete-penetration gas metal arc (GMA) weld was conducted with G3Si1 filler metal wire of 1.2-mm (0.05-in.) diameter, in accordance with DIN EN ISO 14341 (Ref. 17), using a shielding gas mixture of 82% Ar and 18% CO₂ at a flow rate of 18 L/min (4.76 gal/min), in accordance with DIN EN ISO 14175 (Ref. 18). Welding conditions consisted of 261 A welding current, 30.4 V average arc voltage, 8.5 m/min (27.9 ft/min) wire feed rate, and 0.4 m/min (15.7 in./min) travel speed. This resulted in an approximate net heat input of 1 kJ/mm (25.4 kJ/in.). Type-K thermocouple wires with a diameter of 0.5 mm (0.02 in.) were used to acquire the temperature at positions on both the top and bottom of the welded plate directly adjacent to the weld joint. The experimental configuration provided a force-free support of the plate, permitting free shrinkage during the welding process and subsequent cooling. Additionally, a ceramic weld backing was used for all conducted weld experiments.

The residual stresses before and after welding were measured using an Xstress 3000 Goniometer G3 X-ray diffractometer. A 2-mm (0.08-in.) aperture was used, which provided a suitable balance between

time, costs, and results (Ref. 19). The line of measurement across the weld region is represented schematically in Fig. 2.

Experimental Results

Figure 3 shows the experimental weld macrosection with the weld pool area outlined, microstructures at the weld interface, and the HAZ microstructure from a location that experienced a peak temperature of 1159°C (2118°F) and at t_{8/5} time of 30.0 s, where t_{8/5} is the cooling time from 800°C to 500°C. The experimental thermal cycles as measured on both the top and bottom of the welded plate are provided in Fig. 4A. A summary of the individual parameters for each measured thermal cycle is provided in Table 4.

The transverse hardness distribution across the weld region is shown in Fig. 5. The peak hardness of 172 HV₁₀ was found to occur in the weld metal, with a microstructure consisting of mainly Widmanstätten ferrite with aligned second

phase — Fig. 3B. The HAZ microstructure shown in Fig. 3C has a hardness of 162 HV₁₀ and consists of a mixture of grain boundary ferrite, polygonal ferrite, Widmanstätten ferrite with aligned second phase, and ferrite-carbide aggregate. The minimum hardness values, which were below 140 HV₁₀, were found to occur in the base metal region.

The average residual stresses of the plate material after heat treatment were

Table 4 — Summary of Individual Parameters for the Measured Thermal Cycles

Measurement Location	Distance from Weld Centerline (mm)	Peak Temperature (°C)	t _{8/5} Cooling Time (s)
Top of Plate	8.4	953	32
	8.9	795	36 ^(a)
	9.1	765	39 ^(a)
Bottom of Plate	3.9	1159	30
	4.9	1007	30
	6.8	937	30

(a) Extrapolated t_{8/5} cooling times.

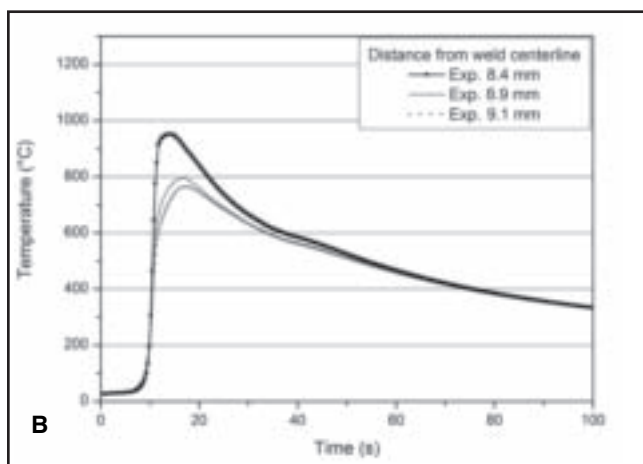
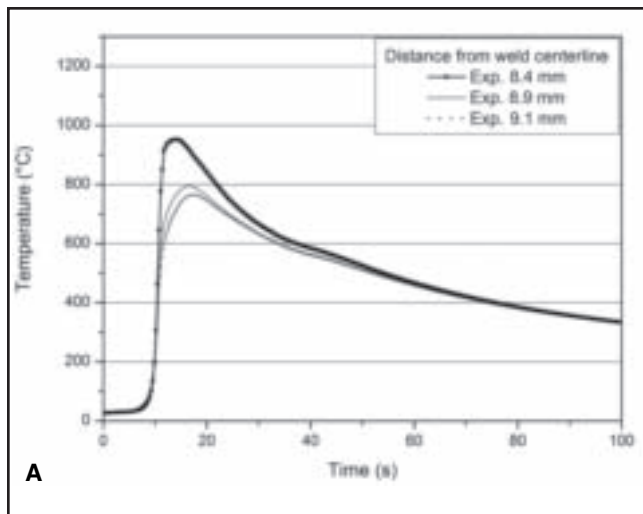


Fig. 4 — Measured thermal cycles adjacent to the weld joint. A — Top of plate; B — bottom of plate.

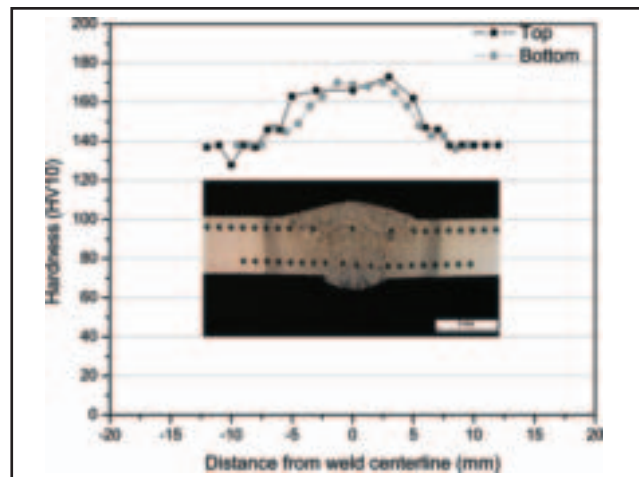


Fig. 5 — Hardness measurements taken along the top and bottom of the experimental weld plate.

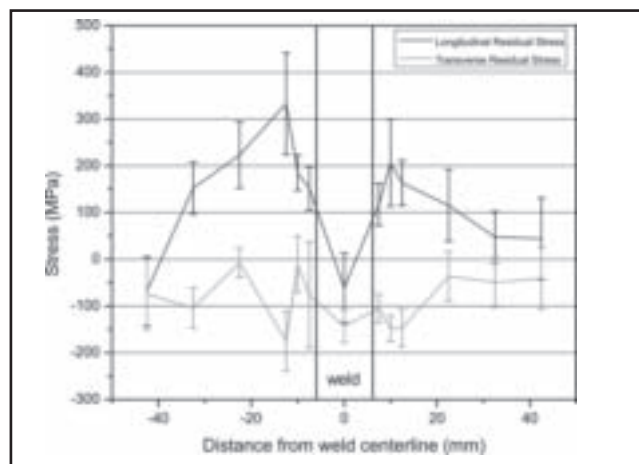


Fig. 6 — Residual stress measurements of experimental weld plate according to line of measurement shown in Fig. 2.

measured to be 21 ± 47 MPa (3.0 ± 6.8 ksi) in the longitudinal direction and 11 ± 45 MPa (1.6 ± 6.5 ksi) in the transverse direction, obtained from 15 measurements. Measurements of both the longitudinal and transverse residual stresses after welding are given in Fig. 6. While a qualitative trend in residual stress is realized, the relatively high error of measurement of each of the points and the differences in the measured values between opposite points equidistant from the weld centerline are noted. The maximum longitudinal residual stress of 333 ± 109 MPa (48.3 ± 15.8 ksi) was measured at a distance of 12.5 mm (0.5 in.) from the weld centerline. At an increasing distance from the weld, the longitudinal residual stresses decrease monotonically down to a stress-free range. The transverse residual stress is compressive in all locations and is mainly constant toward the outer plate region with a minimum stress of -176 ± 64 MPa (-25.5 ± 9.3 ksi) occurring at a distance of 12.5 mm

(0.5 in.) from the weld centerline.

Numerical Simulation Procedure

A complete, self-consistent welding simulation that includes all relevant physical aspects is not yet available. Many couplings are still unknown or not described mathematically, and incorporation of all aspects would result in a very complicated model that is not realistically solvable. Furthermore, the available computational abilities would be limiting for such a complex and demanding task. However, not all aspects need to be known with absolute certainty for reliable calculation and clarification of individual effects (Refs. 20, 21). Welding FE simulations have the ability to separate the influence of the various metallurgical parameters and their effect on the calculated results.

All numerical simulation calculations in this study were performed with the commercial FE software “Sysweld” Version 2008 on a standard PC with a Linux oper-

ating system. The most important simplifications and assumptions of the simulation are as follows:

- Temperature-dependent, homogeneous, and isotropic material properties with consideration of phase transformations.
- A solidus temperature of 1440°C (2624°F) for validation of the weld joint geometry.
- No consideration of preceding process steps; the specimen is assumed to be geometrically ideal and totally stress free, and the weld reinforcement on the top and bottom side are considered.
- Phenomenological temperature field calibration using a combination of a double-elliptical Goldak (Ref. 22) and a 3D-conical Gauss heat source with time-independent volumetric heat flux density and no consideration of weld pool convection.
- Unified heat transfer on all outer surfaces with temperature-dependent radiative

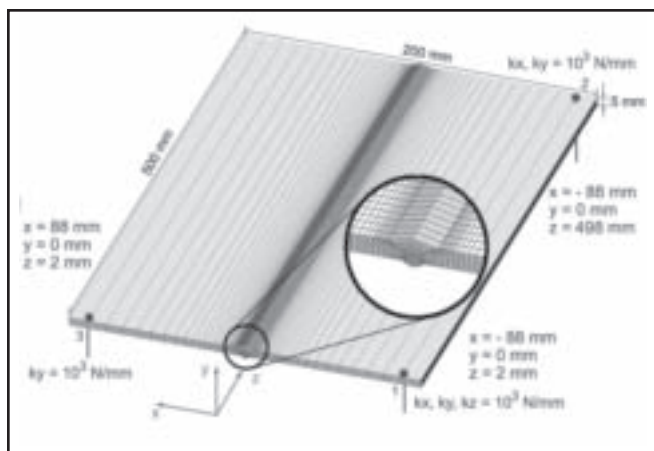


Fig. 7 — Force-free support of the full model for the mechanical calculation. Approximately 90,000 nodes and 94,000 elements.

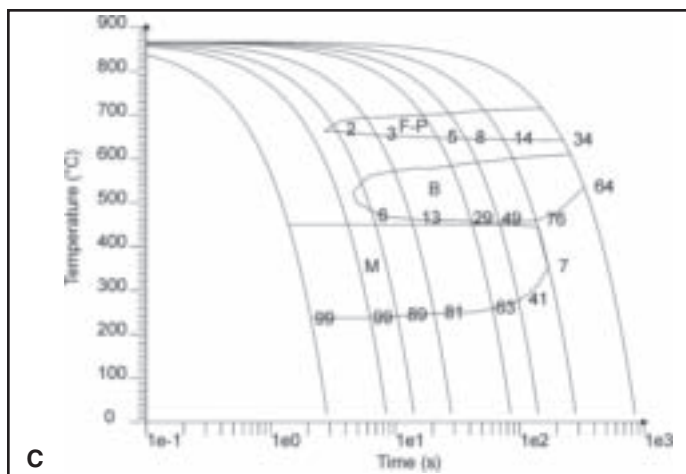
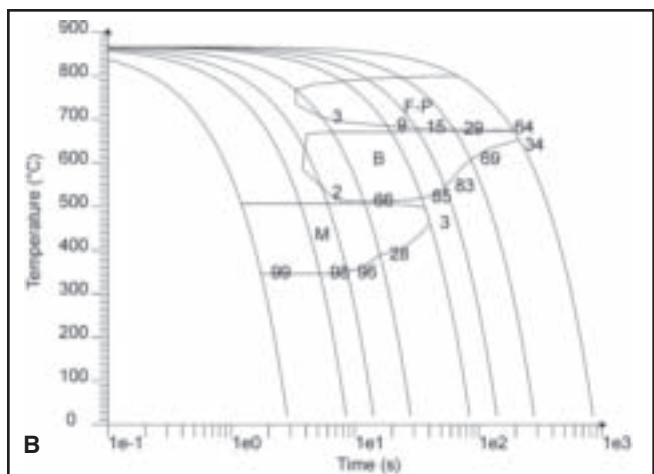
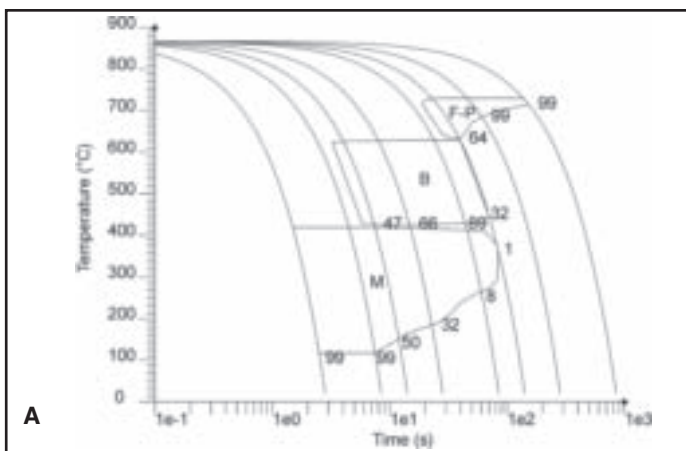


Fig. 8 — CCT diagrams. A — Sysweld metallurgical database; B — Gleeble dilatometry experiments; C — JMatPro TTT/CCT calculations.

losses according to Stefan-Boltzmann, a constant emission coefficient of $\epsilon = 0.8$, constant convective losses of 4 W/mm^2 ($1.27 \times 10^6 \text{ Btu/h}\cdot\text{ft}^2$), and an ambient temperature of 20°C (68°F).

- Idealized clamping of the specimen using elastic constraints of 10^3 N/mm (5715 lbf/in.) for a force-free support.

Finite Element Model

The FE model of the flat plates was meshed as a 3D model corresponding to the experimentally determined temperature gradients. The minimum element length in the weld joint area was 0.37 mm

(0.015 in.) in the Z-X plane and 3 mm (0.12 in.) in the welding direction. The full model used for both the thermal and mechanical simulation consisted of approximately 90,000 nodes and 94,000 elements with a linear basis function. Figure 7 exhibits the FE model geometry used in the thermal welding simulation and the position and the directions of the locked degrees of freedom for the force-free support. The influence of the mesh density on the stiffness of the model was checked in advance. Consequently, in order to obtain an improved bending behavior of the mesh, an increase in the element size further from the weld was not applied.

Thermal Analysis

For the thermal analysis, the experimentally determined data were used to calibrate the heat source of the simulation. Two aspects were considered in the temperature field adjustment. First, the cross-section geometry of the simulated weld pool was correlated with both the size and shape of the experimental macrosection of the weld joint. Second, the corresponding temperature cycles in the HAZ were correlated with the experimental measurements, with emphasis given to peak temperature and cooling time. Each of the simulations was performed with an identi-

Table 5 — Characteristic Phase Transformation Parameters for Each CCT Diagram

CCT Diagram	Phase Transformation Temperatures (°C)				Martensite Temp. Range (°C)	KM Coefficient
	Ferrite/Pearlite Start ^(a)	Bainite Start ^(a)	Martensite Start ^(a)	Martensite Finish		
Sysweld	730	630	420	98	322	0.01428
Gleeble	800	672	508	346	162	0.02843
JMatPro	847/714	634	451	237	214	0.02154

(a) Represents the highest temperature at which the phase is permitted to form.

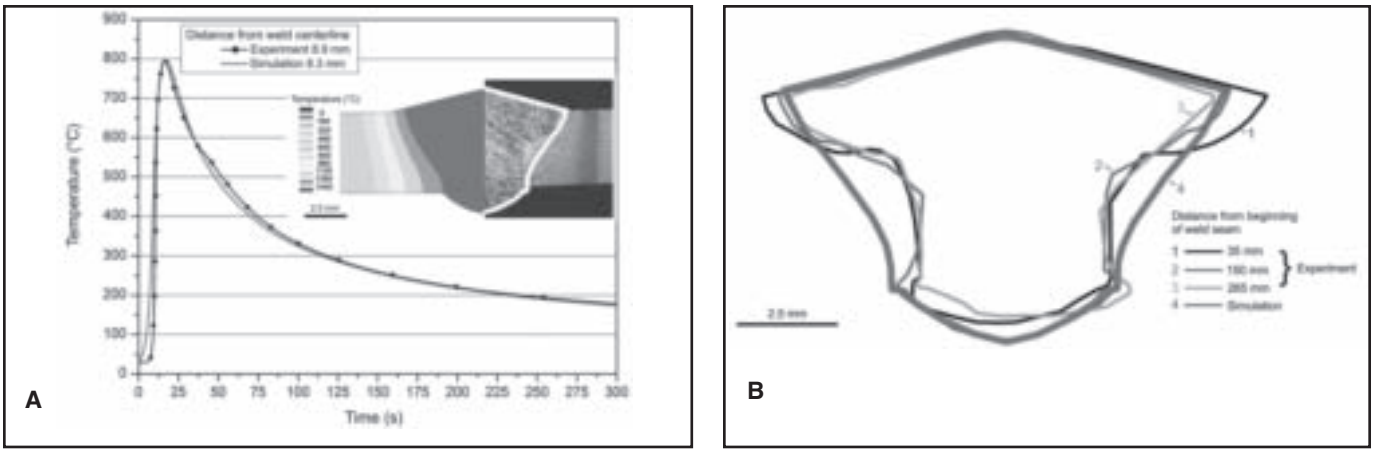


Fig. 9 — A — Validation of the calculated temperature field by thermocouple measurements at top plate position; B — comparison of calculated weld pool outline and experimental macrosections observed at noted locations

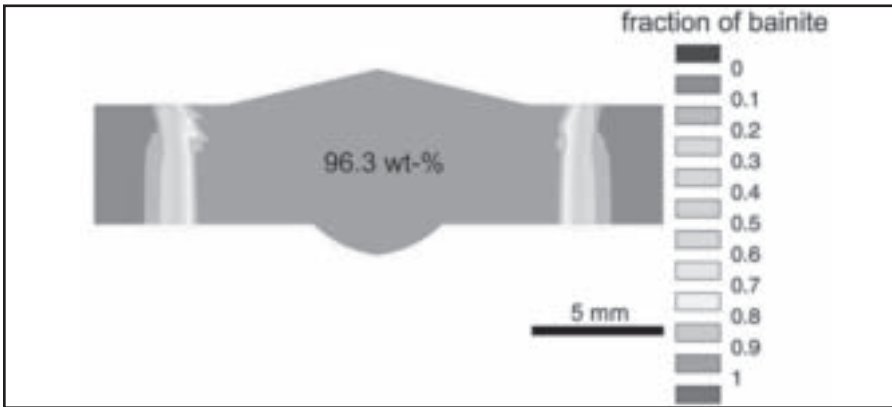


Fig. 10 — Calculated phase fraction of bainite at plate midsection for the Sysweld CCT data.

calibrated temperature field.

Mechanical Analysis

Available in the Sysweld software is the ability to integrate the effect of metallurgical phase transformations in welding simulations. A thermal-metallurgical calculation is first completed using the thermal properties of the material, the calculated temperature field derived and validated from the welding experiments, and the CCT behavior formalized mathematically. The thermal-metallurgical calculation data are then used as an input to the mechanical calculation, which determines stresses and strains according to the transient and spatial distribution of the

previously calculated temperatures in the model. It is noted that this one-way coupling, also referred to as “weak coupling,” does not account for the effect of stress on phase transformation behavior. Furthermore, there is no interaction between the latent heat generated by solid-state phase transformations and the calculated temperature field.

To perform accurate and detailed FE simulations, the thermal and mechanical properties of the material must be known at high temperatures. One of the advantages in selecting the S355J2 alloy was the availability of complete material properties in the Sysweld database, including metallurgical phase transformation temperatures, metallurgical model parameters, and thermo-

physical and thermomechanical properties. The thermophysical and thermomechanical data in the Sysweld database were acquired at various temperatures by previous researchers (Ref. 23). For each of the simulations, an A_{c1} temperature of 727°C (1341°F) and an A_{c3} temperature of 867°C (1593°F) were employed, as stated in the Sysweld material database for S355J2. The residual stresses in the weld metal were not considered in the analysis due to measurement uncertainties, the direct energy input in the respective elements, and the negligence of heat convection in the weld pool.

Metallurgical Model

The general phase transformation model incorporated in the Sysweld software is derived from the Leblond model (Ref. 24) and generalized to account for Johnson-Mehl-Avrami kinetics (Refs. 25–28). The semi-empirical model allows for direct introduction of CCT and TTT data and is represented by the following general equation for transformation of phase i to phase j:

$$\frac{dP_j}{dt} = n(T)F(\dot{T}) \left(\frac{P_{j,eq}(T) - P_j}{\tau(T)} \right)^{n(T)-1} \left[\ln \left(\frac{P_{j,eq}(T)}{P_{j,eq}(T) - P_j} \right) \right]^{n(T)} \quad (1)$$

Table 6 — Calculated Phase Percentages and Vickers Hardness Values for Each CCT Diagram, Referring to a Node with a Peak Temperature of 1300°C and $t_{8/5} = 28$ s

CCT Diagram	Ferrite	Phase, wt-% Bainite	Martensite	Calculated Vickers Hardness ^(a)
Sysweld	0.2	96	3.4	207
Gleeble	6.7	91	2.3	202
JMatPro	5.4	45.5	49	281

(a) Equations provided in Ref. 40.

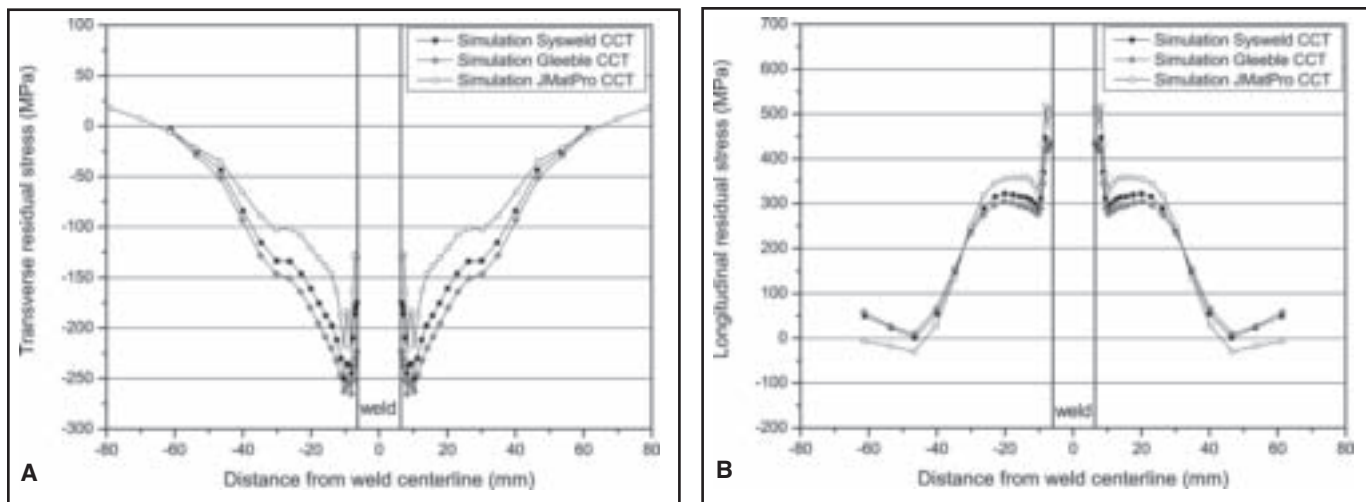


Fig. 11 — Calculated residual stresses as a function of CCT behavior. A — Transverse; B — longitudinal.

where

$P_{j,eq}$ = equilibrium fraction of phase j obtained after an infinite time at temperature T ;

τ = characteristic time constant for the reaction at temperature T ;

n = variable illustrating the reaction rate at temperature T ; and

F = parameter representing cooling rate dependence.

When temperature varies in time, Equation 1 expresses that P_j exponentially approaches $P_{j,eq}$ with time constant equal to τ . The metallurgical parameters τ and n are modeled as piecewise linear functions. For incorporation of experimentally determined CCT data, n is given a nominal value of 1 in the transformation temperature range and Equation 1 simplifies to

$$\frac{dP_j}{dt} = F(\dot{T}) \frac{P_{j,eq}(T) - P_j}{\tau(T)} \quad (2)$$

The parameters τ and F are then manually adjusted to align the predicted phase fraction values with those determined from the experimental CCT data. For introduction of TTT data, parameters τ and n are extracted for various temperatures and incorporated directly into the metallurgical model.

The martensitic transformation is modeled using the Koistinen-Marburger

equation (Ref. 29):

$$P(T) = 1 - \exp(-KM(M_s - T)) \quad (3)$$

where

P = proportion of martensite;

T = temperature;

M_s = martensite start temperature;

KM = Koistinen-Marburger coefficient related to martensitic reaction rate.

The M_s and M_f temperatures are considered to be 0.01 and 0.99 phase fraction transformed, respectively.

Four phases are given consideration in the model: austenite, ferrite-pearlite, bainite, and martensite. The finish temperature of the phase transforming at higher temperature coincides with the start temperature of the phase transforming at a lower temperature.

Metallurgical Model Inputs

Rather than performing an arbitrary adjustment of CCT behavior, three justifiable data sets were used as input to the numerical calculation: data available in the Sysweld database, experimental data acquired through Gleeble dilatometry tests, and TTT/CCT predictions calculated from the JMatPro software. The thermo-physical and thermomechanical properties were identical for the three simulations; only the metallurgical phase

transformation parameters were adjusted.

Sysweld Database

The CCT information available in the Sysweld database for S355J2 was derived from an experimentally determined welding-related CCT diagram (Ref. 30). The CCT diagram was determined by heating samples to a peak temperature of 1350°C (2462°F) and cooling linearly to 850°C (1562°F) before applying different cooling rates to ambient temperature. The composition stated in the Sysweld metallurgical file is the nominal composition for S355J2 as given in the DIN EN 10025-2 standard and presented in Table 1 previously. The CCT diagram implemented in the Sysweld metallurgical file is based on the chemical composition given in Ref. 30 for the S355J2 CCT diagram. It is noted that there is no direct composition adjustment available in the Sysweld software to account for differences in CCT behavior due to compositional differences.

Gleeble Dilatometry Experiments

A set of dilatometry experiments were conducted for S355J2 using a Gleeble 3800 thermal-mechanical simulator. A dilatometer was used to extract dilatation vs. temperature data for several cooling rates. Solid cylindrical samples of diameter 5 mm (0.2 in.) and length 100 mm (3.9 in.) were machined from the experimental S355J2 base plate material. Samples were heated to a peak temperature of 1300°C (2372°F) at 100°C/s (180°F/s) and held at the peak temperature for 1 s before being cooled to 950°C (1742°F) at a rate of 25°C/s (45°F/s). The peak temperature of 1300°C (2372°F) was selected in order to allow for austenite grain growth, promoting a fully martensitic phase transforma-

Table 7 — Residual Stress Values at Ambient Temperature for Each CCT Diagram, Referring to a Node with a Peak Temperature of 1300 °C and $t_{8/5} = 28$ s

CCT Diagram	Transverse (MPa)	Longitudinal (MPa)
Sysweld	-175	434
Gleeble	-224	436
JMatPro	-130	511

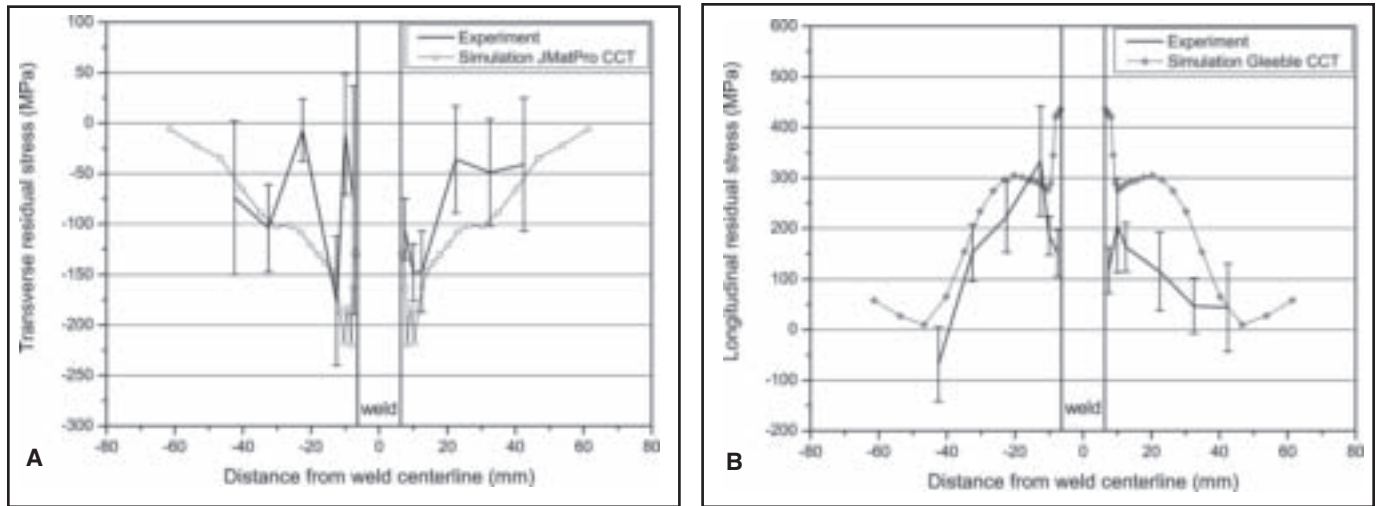


Fig. 12 — Best agreement between experimental and calculated residual stresses. A — Transverse; B — longitudinal.

tion to occur at the fastest cooling rates achievable. Cooling to 950°C (1742°F) was necessary in order to perform a helium gas quench without destroying the sample. The samples were quenched from 950°C (1742°F) at various linear cooling rates. The range of $t_{8/5}$ times achieved was 2.1–23.8 s, with the fastest cooling rates repeated to achieve an average value of transformation temperatures. The CCT determination was made in direct reference to the dilatation data, microstructural evidence, hardness measurements, and to published CCT data for S355J2 (Refs. 30, 31). Following the testing, the dilatation data was analyzed using a linear least squares fitting routine to determine the transformation temperatures and phase fractions. The phase fraction values determined from the dilatation data for individual cooling rates were then used to calibrate the metallurgical model parameters in the Sysweld software.

JMatPro TTT/CCT Calculations

JMatPro is a commercially available software designed to calculate the properties and behavior of multicomponent alloys (Ref. 32). One feature of JMatPro is the calculation of TTT and CCT diagrams of steels, Al alloys, Ni-based superalloys, and Ti alloys. The predicted TTT diagrams for steels are derived from the chemical composition, austenitization temperature, and austenite grain size (Refs. 33, 34). The incorporated phase transformation model is based on the model of Kirkaldy (Ref. 35) and validated with experimentally determined TTT and CCT diagrams (Refs. 36–38). For the TTT calculation, inputs were the composition of S355J2 experimental plate material, as provided in Table 3, an austenitization temperature of 1300°C

(2372°F) and an austenite grain size of 50 μm (0.002 in.), which was selected as an approximate value for the CGHAZ region (Ref. 39). The specific effect of peak temperature and austenite grain size is considered for evaluation in subsequent research. Consistent with the numerical determination of metallurgical parameters outlined in Sysweld, parameters τ and n were determined from the numerical data and directly incorporated in the Sysweld metallurgical model. Since the predicted phase fractions were not directly available from the JMatPro data, Johnson-Mehl-Avrami calculations consistent with the Sysweld metallurgical model were performed for individual cooling rates to obtain the phase fractions. The calculation employed an additivity principle whereby continuous cooling rates were divided into a series of discrete isothermal steps, with the inclusion of a Scheil incubation period (Ref. 40). The calculated phase fraction values for individual cooling rates were then used to calibrate the metallurgical model parameters.

Summary of CCT Diagrams

The three CCT diagrams generated from the mathematically formulized metallurgical data are presented in Fig. 8. From an analysis of the three CCT diagrams, variations are evident in the phase transformation temperatures, the location of the phase transformation regions, and the predicted phase fractions for individual cooling rates. The characteristic phase transformation parameters for the three diagrams are presented in Table 5. The higher M_s temperatures of the Gleeble and JMatPro data may be attributed to the lower level of carbon (0.14 wt-%) in the experimental steel compared to the carbon concentration (0.18 wt-%) of the S355J2 material that was used to

determine the Sysweld CCT diagram by previous researchers (Ref. 30).

For the fastest cooling rates $>100^\circ\text{C/s}$ (180°F/s), all three CCT data sets predict a fully martensitic transformation. Bainite is predicted to begin forming at cooling rates below 100°C/s (180°F/s), with the nose of the bainite curve similarly located in each diagram. However, the bainite transformation kinetics and predicted bainite phase fraction values differ greatly for the three diagrams. For a cooling rate of 60°C/s (108°F/s), the Sysweld database predicts the formation of 47% bainite, while the Gleeble and JMatPro data predict only 2 and 6% bainite, respectively. For a cooling rate of 10°C/s (18°F/s), there is good agreement in the predicted phase fractions between the Sysweld (89% bainite, 8% martensite) and Gleeble (9% ferrite, 85% bainite, 3% martensite) data, with the JMatPro data predicting significantly more martensite (5% ferrite, 29% bainite, 63% martensite). Whereas ferrite-pearlite is predicted to begin forming at cooling rates in the $30^\circ\text{--}60^\circ\text{C/s}$ (54–108°F/s) range for the Gleeble and JMatPro data, the formation of ferrite-pearlite is suppressed to cooling rates below 10°C/s (18°F/s) for the Sysweld data. It is felt that the overall variability of the CCT diagrams investigated is sufficient to reveal the effect of anticipated CCT variations on the calculated residual stresses.

Numerical Simulation Results

Validation of the numerical simulation with experimental data is a necessary requirement to ensure the quality of the calculated results. Figure 9A represents the comparison of a measured and calculated thermal cycle, with the macrosection and

temperature field also shown. The peak temperatures of the simulation thermal cycles were interpolated to exactly match the experimental peak temperatures. As a result, there is some deviation in the exact distances from the weld centerline between experiment and simulation; however, this deviation is in the range of the temperature measurement uncertainty. The experimental $t_{8/5}$ cooling time was approximately 36 s for a peak temperature of 795°C (1463°F). In comparison, the calculated thermal cycle for a peak temperature of 795°C (1463°F) provided a $t_{8/5}$ time of 32 s. The difference of 4 s represents a 12.5% deviation. Regarding the assessed CCT diagrams, no significant microstructural differences are expected for this deviation. Additionally, Fig. 9B shows the calculated weld pool outline in comparison to experimental macrosections of the weld pool shape observed at 35-, 150-, and 265-mm (1.4-, 5.9-, and 10.4-in.) distances from the beginning of the weld joint. The deviation between the average area of the experimental weld pool shape, represented by the area surrounded by the weld interface, and the calculated weld pool outline, represented by the area exceeding the solidus temperature of 1440°C (2624°F), is approximately 9%. This deviation is within the range of deviation of the experimental weld pool macrosection measurements. The validation of the numerically calculated temperature field represents both a good qualitative and quantitative correspondence between the experimental and simulation results. Furthermore, negligible differences were found for both the maximum temperature and temperature gradient of the thermal cycles. Hence, the temperature field provided ensured input data for the subsequent calculation of residual stresses.

Table 6 shows the calculated phase percentages and Vickers hardness values after complete cooling to ambient temperature for a HAZ node nearest to the weld interface experiencing a peak temperature of approximately 1300°C (2372°F). The calculated hardness values were obtained from equations provided in Ref. 41. The phase percentages listed are valid for the weld metal and a major portion of the HAZ, as shown in Fig. 10. This kind of qualitative distribution applies for all three investigated cases because of the identical temperature field that was employed.

Figure 11 exhibits the calculated transverse and longitudinal residual stress distributions for each of the three CCT diagrams considered in the numerical simulation. For all three cases, the transverse residual stresses reach a maximum compressive stress at a distance of 10 mm (0.39 in.) from the weld centerline, with the Gleeble CCT data resulting in the

largest compressive stresses exceeding -250 MPa (-36 ksi). The deviation between the Sysweld and Gleeble results are less than 20 MPa (3 ksi), except for the values directly adjacent to the weld interface where larger deviations occur. The calculations based on the JMatPro CCT data result in the highest longitudinal residual stresses, reaching a peak above 500 MPa (73 ksi) near the weld interface. At distances of 10–30 mm from the weld centerline, a plateau of approximately 300–350 MPa (44–51 ksi) is noted, followed by a monotonic decrease to a stress-free level. Table 7 provides a summary of the calculated residual stress values for a node adjacent to the weld interface.

Discussion

Comparing the experimental measurements and calculated residual stresses, a qualitative correlation only was realized in both the transverse and longitudinal directions, with the largest deviation occurring in the HAZ region nearest to the weld interface. The JMatPro CCT exhibited the best agreement with the measured transverse residual stress distribution — Fig. 12A. Considering the longitudinal residual stresses, the Gleeble CCT provided the best agreement with the experimental values — Fig. 12B. The discrepancy in stress values may be attributed to the uncertainty associated with the residual stress measurements as noted previously, simplifying assumptions of the numerical simulation, and significant differences between the phase percentages of the experimental microstructures and those predicted by the CCT data, as discussed in the following paragraph.

Referring to Table 6, it can be seen that the calculated Vickers hardness values are higher than the experimental measurements as shown in Fig. 5. The Sysweld and Gleeble CCT resulted in calculated hardness values slightly above 200 HV, while the calculated hardness of the JMatPro CCT was found to be 281 HV. The average measured hardness of the experimental microstructures in the weld metal and CGHAZ regions was found to be 166 HV10. Using the equations in Ref. 41 as a guide, the experimental microstructure with this hardness value is estimated to consist of approximately 50% ferrite and 50% bainite, assuming a negligible amount of martensite. Overall, the lower hardness of the experimental microstructure can be attributed to a higher proportion of ferrite, as evidenced in Fig. 3B and C. Due to its lower yield strength, a higher proportion of ferrite in the experimental microstructure would contribute to lowering the longitudinal residual stresses measured near the weld interface in comparison to the calculated stress values. The

higher yield strength associated with a higher proportion of martensite would contribute to increasing the maximum potential residual stress.

Notwithstanding the noted differences between the experimental and calculated residual stress values, a determination of the effect of CCT variations on the calculated residual stresses is the main point of investigation. As shown in Fig. 11, the calculated residual stresses exhibit a similar qualitative distribution for each of the three CCT diagrams investigated. The largest deviation between the three cases was found to occur in the HAZ region nearest to the weld interface. Referring to Table 7, the stress values calculated for a node nearest to the weld interface vary from -224 to -130 MPa (-32 to -19 ksi) in the transverse direction and 434 to 511 MPa (63 to 74 ksi) in the longitudinal direction. This represents a relatively small deviation between the three cases, and suggests that only minimal losses in accuracy are to be expected for the level of CCT variations investigated in this study.

A microstructural comparison shows the most significant effect on the calculated residual stresses to be related to the proportion of formed martensite. The small deviation between the Sysweld and Gleeble stress distributions correlates with the microstructural similarity between the two cases (Table 6), where less than 5% martensite is predicted to form in each case. For the JMatPro CCT case, 49% martensite is predicted to form in the microstructure, which supports the larger deviation in stress distribution in comparison to those calculated with the Sysweld and Gleeble CCT data. The higher martensite proportion for the JMatPro CCT was shown to decrease the compressive transverse stresses and increase the tensile longitudinal stresses throughout the HAZ region. Specific investigation regarding the influence of the martensite transformation on the calculated residual stresses is planned for future work.

Conclusions

1. A qualitative correlation only was realized between the experimental residual stress measurements and the calculated residual stresses in both the transverse and longitudinal directions. The discrepancy in stress values is attributed to residual stress measurement uncertainty, simplifying assumptions of the numerical simulation, and significant differences between the phase percentages of the experimental microstructures and those predicted by the CCT data.

2. For the S355J2 steel investigated and the employed numerical simulation approach, there was shown to be an overall weak dependency of the calculated residual stresses due to anticipated variations

in CCT behavior. The maximum deviation in the calculated stresses for the three CCT diagrams investigated was -224 to -130 MPa (-32.5 to -19 ksi) in the transverse direction and 434 to 511 MPa (-63 to -74 ksi) in the longitudinal direction. These results suggest that CCT data of approximate accuracy, in combination with detailed material property data, is sufficient for reliable calculation of welding-induced residual stresses.

3. The most significant effect of CCT variations on the calculated residual stress distributions was related to the proportion of formed martensite. A higher martensite proportion was shown to decrease the compressive transverse stresses and increase the tensile longitudinal stresses throughout the HAZ region.

Acknowledgments

The authors gratefully acknowledge the financial support for this research from the German Federal Ministry of Economics and Technology (BMWi) within the framework program of the "Innovation with Norms and Standards (INS)" coordinated and conducted by the German Institute for Standardization (DIN). The respective INS-project, "Draft guideline for a structured approach for the execution, analysis and postprocessing of a numerical simulation of welding induced distortions and residual stresses," was coordinated by the DIN Welding Standards Committee (NAS).

References

- Withers, P. J., and Bhadeshia, H. K. D. H. 2001. Residual stress Part 2 — Nature and origins. *Materials Science and Technology* 17: 366–375.
- Jones, W. K. C., and Alberry, P. J. 1977. A model for stress accumulation of steels during welding. *International Conference on Residual Stresses in Welded Construction and Their Effects*. London, UK: The Welding Institute, pp. 15–26.
- Kannengiesser, T., Boellinghaus, T., and Neuhaus, M. 2006. Effects of the load history on the residual stress distribution in welded components. *Welding in the World* 50(7/8): 11–17.
- Dong, P. 2005. Residual stresses and distortions in welded structures: A perspective for engineering applications. *Science and Technology of Welding and Joining* 10(4): 389–398.
- Ueda, Y., Fukuda, K., and Nakacho, K. 1977. Basic procedures in analysis and measurement of welding residual stresses by the finite element method. *Residual Stresses in Welded Constructions and Their Effects*, pp. 27–37. Abrington Verlag.
- Karlsson, L., Lindgren, L. E., Jonson, M., Josefson, L., and Oddy, A. 1997. Modelling of residual stresses and distortion development. *Mathematical Modelling of Weld Phenomena 3*, eds. H. K. D. H. Bhadeshia and H. Cerjak, pp. 571–589. The Institute of Materials.
- Taljat, B., Radhakrishnan, B., and Zacharia, T. 1998. Numerical analysis of GTA welding process with emphasis on post-solidification phase transformation effects on residual stresses. *Materials Science and Engineering A*, pp. 45–54.
- Ferro, P., Porzner, H., Tiziani, A., and Bonollo, F. 2006. The influence of phase transformations on residual stresses induced by the welding process — 3D and 2D numerical models. *Modelling and Simulation in Materials Science and Engineering* 14: 117–136.
- Mochizuki, M., and Toyoda, M. 2007. Strategy of considering microstructure effect on weld residual stress analysis. *Journal of Pressure Vessel Technology* 129: 619–629.
- Dean, D., and Hidekazu, M. 2006. Prediction of welding residual stress in multi-pass butt-welded modified 9CR-1MO steel pipe considering phase transformation effects. *Computational Materials Science* 37: 209–219.
- Schwenk, C., Rethmeier, M., Dilger, K., and Michailov, V. 2007. Sensitivity analysis of welding simulation depending on material properties value variation. *Mathematical Modelling of Weld Phenomena 8*, eds. H. K. D. H. Bhadeshia, E. Kozeschnik, and H. Cerjak, pp. 1107–1128. Verlag der Technischen Universität Graz.
- Payares-Asprino, M. C., Katsumoto, H., and Liu, S. 2008. Effect of martensite start and finish temperature on residual stress development in structural steel welds. *Welding Journal* (87)11: 278-s to 289-s.
- Francis, J. A., Bhadeshia, H. K. D. H., and Withers, P. J. 2007. Welding residual stresses in ferritic power plant steels. *Materials Science and Technology* 23(9): 1009–1020.
- Krauss, G. 2005. *Steels: Processing, Structure, and Performance*. Materials Park, Ohio: ASM International.
- Harrison, P. L., and Farrar, R. A. 1989. Application of continuous cooling transformation diagrams for welding of steels. *International Materials Review* 34(1): 35–51.
- DIN EN 10025-2:2005, *Hot Rolled Structural Steel Products — Part 2: Technical Specifications for Unalloyed Structural Steels*. Deutsches Institut für Normung e.V., Berlin. 2005.
- DIN EN 14341:2008: *Welding Consumables — GMAW Electrodes for Unalloyed and Fine Grain Steels*. Deutsches Institut für Normung e.V., Berlin. 2008.
- DIN EN ISO 14175:2008: *Welding Consumables — Gases and Gas Mixtures for Arc Welding and Related Processes*. Deutsches Institut für Normung e.V., Berlin. 2008.
- Hauk, V. 1997. *Structural and Residual Stress Analysis by Nondestructive Methods*. Elsevier.
- Lindgren, L. E. 2002. Modelling for residual stresses and deformations due to welding — Knowing what isn't necessary to know. *Mathematical Modelling of Weld Phenomena 6*, eds. H. K. D. H. Bhadeshia and H. Cerjak. The Institute of Materials, pp. 491–518.
- Radaj, D., Lundbäck, A., and Lindgren, L. E. 2007. Verification and validation in computational welding mechanics. In *Mathematical Modelling of Weld Phenomena 8*, eds. H.K.D.H. Bhadeshia, E. Kozeschnik, and H. Cerjak. Verlag der Technischen Universität Graz, pp. 1039–1051.
- Goldak, J., Chakravarti, A., and Bibby, M. 1984. A new finite element model for welding heat-sources. *Metallurgical Transactions B* 15B(2): 299–305.
- Voß, O. 2001. Investigation of factors' significance on numerical simulation of welds. PhD thesis. Technical University, Braunschweig, Shaker.
- Leblond, J. B., and Devaux, J. 1984. A new kinetic model for anisothermal metallurgical transformations in steels including effect of austenite grain size. *Acta Metallurgica* 32(1): 137–146.
- Johnson, W. A., and Mehl, R. F. 1939. Reaction kinetics in process of nucleation and growth. *Transactions AIME* 135: 416–458.
- Avrami, M. 1939. Kinetics of phase change I: General theory. *Journal of Chemical Physics* 7: 103–112.
- Avrami, M. 1940. Kinetics of phase change II: Transformation-time relations for random distribution of nuclei. *Journal of Chemical Physics* 8: 212–224.
- Avrami, M. 1941. Kinetics of phase change III: Granulation, phase change, and microstructure. *Journal of Chemical Physics* 9: 177–184.
- Koistinen, D. P., and Marburger, R. E. 1959. A general equation prescribing the extent of the austenite-martensite transformation in pure iron-carbon alloys and plain carbon steels. *Acta Metallurgica* pp. 59–60.
- Seyffarth, P., Meyer, B., and Scharff, A. 1992. *Compendium of Welding ZTU Photographs*. Deutscher Verlag für Schweißtechnik DVS-Verlag GmbH.
- Berkout, C. F., and van Lent, P. H. 1968. Application of cooling rate from peak temperatures — Photographs from welding of high strength steels. *Schweißen und Schneiden* 20(6): 256–260.
- Saunders, N., Guo, Z., Li, X., Miodownik, A. P., and Schille, J. P. 2003. Using JMatPro to model materials properties and behavior. *Journal of Materials* 55(12): 60–65.
- Saunders, N., Guo, Z., Li, X., Miodownik, A. P., and Schille, J. P. The calculation of TTT and CCT diagrams for general steels. JMatPro Software Literature.
- Guo, Z., Saunders, N., Miodownik, A. P., and Schille, J. P. 2006. Modelling material properties leading to the prediction of distortion during heat treatment of steels. *Materials Science and Technology*.
- Kirkaldy, J. S., Thomson, B. A., and Baganis, E. A. 1978. *Hardenability Concepts with Applications to Steel*, eds. J. S. Kirkaldy and D. V. Doane.
- Atlas of Isothermal Transformation Diagrams of BS En Steels*. 1956. The Iron and Steel Institute.
- Atlas of Isothermal and Cooling Transformation Diagrams*. 1977. Metals Park, Ohio: ASM International.
- Atkins, M. 1977. *Atlas of Continuous Cooling Transformation Diagrams for Engineering Steels*. British Steel Corp.
- Easterling, K. E. 1992. *Introduction to the Physical Metallurgy of Welding*. 2nd Edition. Butterworth-Heinemann.
- Scheil, E. 1935. Start of phase transformation to austenite. *Arch. Eisenhüttenw* 8: 565–567.
- Blondeau, R., Maynier, P., and Dollet, J. 1973. Prediction of hardness and strength of carbon steels and low alloys according to their structure and composition. *Mem. Sci. Rev. Metallurgy* 70(12): 883–892.